# Modeling and simulation of needle electrical impedance myography in nonhomogeneous isotropic skeletal muscle

Xuesong Luo, Shaoping Wang and Benjamin Sanchez, *Senior Member, IEEE*

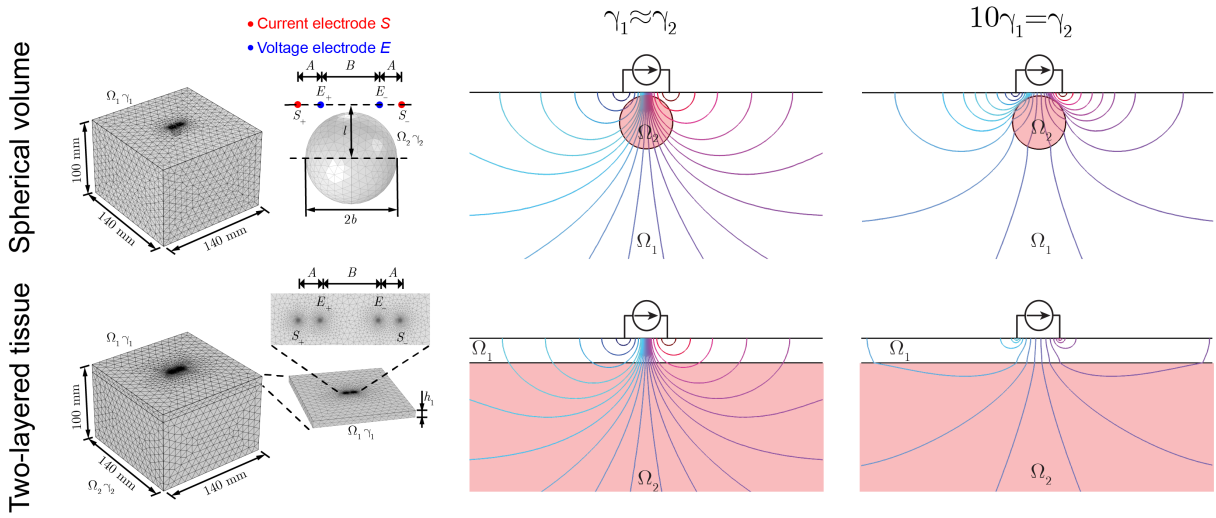


Nonhomogeneous finite element model simulations illustrate the distortion in the spatial distribution of the isopotential lines within the domain $\Omega_1$ due to the vicinity of the domain $\Omega_2$ with different conductivity and permittivity properties.

## Take-Home Messages

- Low-frequency electromagnetics principles have been applied to develop a novel framework to interpret electrical impedance myography measurements in nonhomogeneous muscle
- Our theoretical framework will lead to new ways for interpreting EIM data with direct clinical application for neuromuscular evaluation
- Electrical impedance myography evaluation of patients with neuromuscular disorders
- Our framework provides the means to advance our understanding of needle EIM outcomes in nonhomogeneous diseased muscle
- Finite element method simulations confirm the usefulness of our electrostatic framework for predicting EIM in diseased muscle

# Modeling and simulation of needle electrical impedance myography in nonhomogeneous isotropic skeletal muscle

Xuesong Luo, Shaoping Wang and Benjamin Sanchez, *Senior Member, IEEE*

***Abstract*—*Objective*: Needle electrical impedance myography (EIM) is a recently developed technique for neuromuscular evaluation. Despite its preliminary successful clinical application, further understanding is needed to aid interpreting EIM outcomes in nonhomogeneous skeletal muscle measurements. *Methods*: The framework presented models needle EIM measurements in a bidomain isotropic model. Finite element method (FEM) simulations verify the validity of our model predictions studying two cases: a spherical volume surrounded by tissue and a two-layered tissue. *Results*: Our models show that EIM is influenced by the vicinity of tissue with different electrical properties. The apparent resistance, reactance and phase relative errors between our theoretical predictions and FEM simulations in the spherical volume case study are $\leq$0.2%, $\leq$1.2% and $\leq$1.0%, respectively. For the two-layered tissue model case study, the relative errors are $\leq$2%. *Conclusions*: We propose a bio-physics driven analytical framework describing needle EIM measurements in a nonhomogeneous bidomain tissue model. *Clinical impact*: Our theoretical predictions may lead to new ways for interpreting needle EIM data in neuromuscular diseases that cause compositional changes in muscle content, e.g. connective tissue deposition within the muscle. These changes will manifest themselves by changing the electric properties of the conductor media and will impact impedance values.**

***Keywords*—Needle electrical impedance myography (EIM), nonhomogeneous tissue, skeletal muscle, neuromuscular disorders.**

## I. Introduction

NEEDLE electrical impedance myography (EIM) is a relatively new technique to evaluate skeletal muscle health [1]. Unlike EIM approaches using surface electrodes [2], the working principle of needle EIM consists of inserting a needle into the muscle for electrical impedance recording [3]. Alterations in the muscle composition and structure caused by a broad range of neuromuscular conditions change how the current flows through the muscle and thus alter the measured voltages and the resultant EIM values [4]–[6]. Needle EIM approaches rely upon low-frequency electrostatic principles. Namely, the electrical current that is applied to the muscle is altered as a function of the frequency due to the inherent electrical properties of the muscle (namely the conductivity and the relative permittivity properties) and their changes associated with disease [7].

First needle EIM studies have shown the potential value of the technique to assess impedance changes in healthy and dystrophic muscle in rodent animal models [8]. More recently, we evaluated the reproducibility and safety of needle EIM measuring patients with a broad range of neuromuscular disorders [9]. Needle theoretical models and FEM simulations revealed good agreement with maximum experimental errors $<$10%. Patient inter-session reproducibility also was promising with intraclass correlation coefficients of 0.926, which is comparable or exceeds the reproducibility of other well-established electrophysiological tests to assess muscle health [10], [11].

X. Luo and S. Wang are with the Department of Automation Science and Electric Engineering, Beijing Advanced Innovation Center for Big Data-Based Precision Medicine, Beihang University, Beijing 100083, China.

X. Luo and B. Sanchez are with the Sanchez Research Lab, Department of Electrical and Computer Engineering, Sorenson Molecular Biotechnology Building, 36 South Wasatch Drive, University of Utah, Salt Lake City, UT 84112, USA, email: benjamin.sanchez@utah.edu. Corresponding author's phone: (801) 585-9535, email: benjamin.sanchez@utah.edu

Importantly, the pathogenesis of neuromuscular disorders such as amyotrophic lateral sclerosis [12], Duchenne muscular dystrophy [13] and facioscapulohumeral muscular dystrophy [14] are known to induce major changes in muscle structure and composition including the deposition of connective tissue, fat infiltration and pockets of inflammatory cells within the tissue. Therefore, the presence of these tissues with known different electrical properties [15] in the vicinity where the EIM needle is inserted will likely impact needle EIM data. To further refine needle EIM and be able to provide clinically meaningful outcomes is thus necessary to advance our current understanding on how sensitive needle EIM is to changes in electrical properties in nonhomogeneous diseased muscle.

This article aims to expand to our theoretical understanding of needle EIM recordings in nonhomogeneous diseased muscle tissue. To do that, we first define the physics' setting for needle EIM measurement in Sections II and III. Using the generalized Poisson equation describing the distribution of electrical potential within muscle. Unlike previous studies that modeled electrical potential caused by transmembrane current, e.g, due to fiber membrane depolarization [16]–[18], here the potential is generated by the external application of electrical current required to measure EIM. Next, we derive a physical plausible model to describe the tissue impedance based on the muscle electrical properties and domain. We studied two specific cases modeling needle EIM: spherical model representing fat deposition within the muscle and a two-layered model to study the effect of subcutaneous fat affecting the measurement for example. These mathematical models were validated with electrostatic simulations by comparing the apparent impedance values. Section IV describes the methods and simulation results in Section V confirm the usefulness of the novel approach presented. Finally, the main findings are discussed in Section VI and summarized in the form of

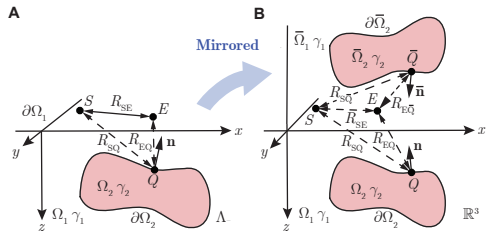


Fig. 1. Schematic illustrating a nonhomogeneous tissue modeled as a bidomain in $\Lambda_-$ (A) and mirrored image in $\mathbb{R}^3$ (B). The domain $\Omega_2$ enclosed by the boundary $\partial\Omega_2$ and isotropic admittivity $\gamma_2$ is contained in the domain $\Omega_1$ with isotropic admittivity $\gamma_1$. The boundary of $\Omega_1$ is the plane $\partial\Omega_1 := (x, y, 0)$ in (A). The point current source $S$ located at $\mathbf{r}_\mathrm{S} := (x_\mathrm{S}, y_\mathrm{S}, 0)$ on $\partial\Omega_1$ generates electrical current and $E$ located at $\mathbf{r}_\mathrm{E} := (x_\mathrm{E}, y_\mathrm{E}, 0)$ is an arbitrary point on $\partial\Omega_1$ where we want to determine the electrical potential. The point $Q$ with coordinates $\mathbf{r}_\mathrm{Q} := (x_\mathrm{Q}, y_\mathrm{Q}, z_\mathrm{Q})$ is on $\partial\Omega_2$ and $\mathbf{n}$ is the outward normal vector at $Q$. $R_\mathrm{SE}$ is the distance between $S$ and $E$; $R_\mathrm{SQ}$ is the distance between $S$ and $Q$; $R_\mathrm{EQ}$ is the distance between $E$ and $Q$. The half space model $\Lambda_-$ in (A) is mirrored with respect to $\partial\Omega_1$ and forms the mirrored full space $\mathbb{R}^3$ (B). All mirrored elements in (B) are overlined to distinguish from their nonmirrored counterparts in (A).

conclusions in Section VII.

## II. Bidomain tissue model in half space

We consider a nonhomogeneous tissue modeled as a bidomain space (Figure 1A) [19]. The model in half space $\Lambda_-$ in $\mathbb{R}^3_-$ contains domains $\Omega_1$ and $\Omega_2$, so that $\Lambda_- := \Omega_1 \cup \Omega_2$ and $\Omega_1 \cap \Omega_2 = \partial\Omega_2$. The boundaries of $\Omega_1$, $\Omega_2$ are $\partial\Omega_1$ (plane $z = 0$) and $\partial\Omega_2$ (arbitrary surface), respectively. We define $\mathbf{r} := (x, y, z)$ a position in $\Lambda_-$. In this model, we consider a surface current source $S$ located at $\mathbf{r}_\mathrm{S} := (x_\mathrm{S}, y_\mathrm{S}, 0)$ that generates a sinusoidal electrical current of amplitude $I \in \mathbb{R}$ (A) at (angular) frequency $\omega_k \in \mathbb{R}$ (rad s$^{-1}$) with current sink at infinity. Henceforth, we assume the current source and voltage measuring electrodes are point-like electrodes, the domains are isotropic with constant electrical properties, there are no free charges, and the model is in the vacuum (i.e., the electrical current cannot flow out of the model).

### A. Governing equation

The admittivity $\gamma \in \mathbb{C}$ (S m$^{-1}$) of the nonhomogeneous model depends on the position $\mathbf{r}$ and measurement frequency $\omega_k$ and is expressed explicitly as

$$\gamma(\mathbf{r}, \omega_k) := \gamma_1(\omega_k) H(\mathbf{r} - \mathbf{n}) + \gamma_2(\omega_k) H(\mathbf{r} + \mathbf{n}), \tag{1}$$

where $H(\bullet)$ is the Heaviside unit step function, $\mathbf{n}$ is the outward normal vector at $Q$; then $\gamma_{1,2}(\omega_k) := \sigma_{1,2}(\omega_k) + j\omega_k \varepsilon_{1,2}(\omega_k)$, where $\sigma_{1,2} \in \mathbb{R}_{>0}$ is the conductivity (S m$^{-1}$), $\varepsilon_{1,2} \in \mathbb{R}_{>0}$ is the permittivity (F m$^{-1}$), $\gamma_1$ is in $\Omega_1$ and $\gamma_2$ is in $\Omega_2$, $j = \sqrt{-1}$ is the imaginary unit (dimensionless). From low frequency Maxwell equations in quasistationary regime [20], the electrical potential $U(\mathbf{r}, \omega_k) \in \mathbb{C}$ (V) is described by the generalized Poisson equation

$$\nabla \cdot [\gamma(\mathbf{r}, \omega_k) \nabla U(\mathbf{r}, \omega_k)] = -I\delta(\mathbf{r} - \mathbf{r}_\mathrm{S}), \tag{2}$$

where $\delta(\mathbf{r})$ is the Dirac delta function.

For clarity in the notation, henceforth we omit the position and frequency dependence of the admittivity and electrical potential. Using the half-maximum convention we have $H(\mathbf{0}) = 1/2$, then the admittivity on $\partial\Omega_2$ is $(\gamma_1 + \gamma_2)/2$ from (1). Noting that $\nabla H(\mathbf{r}) = \delta(\mathbf{r})$, we can rewrite (2) as follows

$$\nabla^2 U = -\frac{I\delta(\mathbf{r} - \mathbf{r}_\mathrm{S})}{\gamma} - 2\Gamma\delta(\partial\Omega_2)\frac{\partial U}{\partial \mathbf{n}} \cdot \mathbf{n}, \tag{3}$$

where $\Gamma := (\gamma_1 - \gamma_2)/(\gamma_1 + \gamma_2) \in \mathbb{C}$ (dimensionless) is known as the reflection coefficient.

The boundary condition of $\Lambda_-$ is

$$\left.\frac{\partial U}{\partial z}\right|_{\partial\Omega_1} = 0.$$

To satisfy this boundary condition, we use the method of images charges in (3) [21] (Figure 1B). Then, (3) can be modified to include the image reflection term, namely

$$\begin{aligned}\nabla^2 U = &-\frac{2I\delta(\mathbf{r} - \mathbf{r}_\mathrm{S})}{\gamma} - 2\Gamma \\ &\cdot \left(\delta(\partial\Omega_2)\frac{\partial U}{\partial \mathbf{n}} \cdot \mathbf{n} + \delta(\partial\overline{\Omega}_2)\frac{\partial U}{\partial \overline{\mathbf{n}}} \cdot \overline{\mathbf{n}}\right),\end{aligned} \tag{4}$$

where all overlined valuables are mirrored elements from nonoverlined counterparts by plane $z = 0$.

### B. Electrical potential distribution

To solve (4), we use the method of Green's function to obtain the integral expression of the electrical potential [22], i.e.,

$$\begin{cases} U(\mathbf{r}) &= U_0(\mathbf{r}) + U_{\Omega_2}(\mathbf{r}) \\ U_0(\mathbf{r}) &= \frac{I}{2\pi\gamma_1|\mathbf{r} - \mathbf{r}_\mathrm{S}|} \\ U_{\Omega_2}(\mathbf{r}) &= \frac{\Gamma}{2\pi}\iint_{\partial\Omega_2} \frac{\partial U(\mathbf{r}_\mathrm{Q})}{\partial \mathbf{n}} \cdot \mathbf{n} \frac{\mathrm{d}(\partial\Omega_2)}{|\mathbf{r} - \mathbf{r}_\mathrm{Q}|} \\ &\quad + \frac{\Gamma}{2\pi}\iint_{\partial\overline{\Omega}_2} \frac{\partial U(\mathbf{r}_{\overline{\mathrm{Q}}})}{\partial \overline{\mathbf{n}}} \cdot \overline{\mathbf{n}} \frac{\mathrm{d}(\partial\overline{\Omega}_2)}{|\mathbf{r} - \mathbf{r}_{\overline{\mathrm{Q}}}|}, \end{cases} \tag{5}$$

where $\mathbf{r} \neq \mathbf{r}_\mathrm{S}$, $Q$ is arbitrary point with coordinates $\mathbf{r}_\mathrm{Q} := (x_\mathrm{Q}, y_\mathrm{Q}, z_\mathrm{Q})$ on $\partial\Omega_2$, the operator $|\cdot|$ is the $L_2$ norm , $\mathrm{d}(\partial\Omega_2)$ and $\mathrm{d}(\partial\overline{\Omega}_2)$ represent the area of the micro-elements $\partial\Omega_2$ and $\partial\overline{\Omega}_2$ at $Q$ and $\overline{Q}$, respectively. Next we define the $p$th-order approximated (denoted by $\widetilde{\ }$) electrical potential distribution $\widetilde{U}^{(p)} \in \mathbb{C}$ (V) following the same rationale as in [23]

$$\begin{cases} \widetilde{U}^{(p)}(\mathbf{r}) &:= U_0(\mathbf{r}) + \widetilde{U}^{(p)}_{\Omega_2}(\mathbf{r}) \\ \widetilde{U}^{(0)}(\mathbf{r}) &:= U_0(\mathbf{r}), \\ \widetilde{U}^{(p)}_{\Omega_2}(\mathbf{r}) &:= \frac{\Gamma}{2\pi}\iint_{\partial\Omega_2} \frac{\partial \widetilde{U}^{(p-1)}(\mathbf{r}_\mathrm{Q})}{\partial \mathbf{n}} \cdot \mathbf{n} \frac{\mathrm{d}(\partial\Omega_2)}{|\mathbf{r} - \mathbf{r}_\mathrm{Q}|} \\ &\quad + \frac{\Gamma}{2\pi}\iint_{\partial\overline{\Omega}_2} \frac{\partial \widetilde{U}^{(p-1)}(\mathbf{r}_{\overline{\mathrm{Q}}})}{\partial \overline{\mathbf{n}}} \cdot \overline{\mathbf{n}} \frac{\mathrm{d}(\partial\overline{\Omega}_2)}{|\mathbf{r} - \mathbf{r}_{\overline{\mathrm{Q}}}|} \end{cases} \tag{6}$$

where $p \in \mathbb{N}_{>0}$ is the order of the approximation, $|\Gamma| < 1$ and $U = \lim_{p\to\infty} \widetilde{U}^{(p)}$.

With the surface voltage recording electrode $E$ at $\mathbf{r}_\mathrm{E} := (x_\mathrm{E}, y_\mathrm{E}, 0)$ (see Figure 1A), the model can be simplified based on symmetry of image (Figure 1 B). According to (6), the electrical potential recorded by electrode $E$ is

$$\widetilde{U}^{(1)}(\mathbf{r}_\mathrm{E}) = \frac{I}{2\pi\gamma_1}\left(\frac{1}{R_\mathrm{SE}} + 2K_{\Omega_2}\Gamma\right), \tag{7}$$

where

$$K_{\Omega_2} := -\frac{1}{2\pi}\iint_{\partial\Omega_2} \frac{\partial R_\mathrm{SQ}(\mathbf{r}_\mathrm{Q})}{\partial \mathbf{n}} \cdot \mathbf{n} \frac{\mathrm{d}(\partial\Omega_2)}{R^2_\mathrm{SQ}(\mathbf{r}_\mathrm{Q}) R_\mathrm{EQ}(\mathbf{r}_\mathrm{Q})}$$

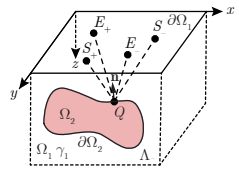


Fig. 2. Schematic illustrating a tetrapolar electrical impedance measurement in a nonhomogeneous bidomain model in $\Lambda_-$. The admittivity of the domain $\Omega_1$ and $\Omega_2$ and their boundary are $\gamma_1$, $\gamma_2$, $\partial\Omega_1 := (x,y,0)$ and $\partial\Omega_2$, respectively. $Q$ is an arbitrary point on $\partial\Omega_2$ and $\mathbf{n}$ is the outward normal vector at $Q$. The current source (+) and sink (−) electrodes are $S_\pm$ and the high (+) and low (−) voltage measuring electrodes are $E_\pm$ placed on $\partial\Omega_1$.

is a geometrical constant ($\mathrm{m}^{-1}$) determined by the shape and position of $\Omega_2$, $R_{\mathrm{SE}} := |\mathbf{r}_{\mathrm{S}} - \mathbf{r}_{\mathrm{E}}|$ (m); $R_{\mathrm{SQ}} := |\mathbf{r}_{\mathrm{S}} - \mathbf{r}_{\mathrm{Q}}|$ (m); and $R_{\mathrm{EQ}} := |\mathbf{r}_{\mathrm{E}} - \mathbf{r}_{\mathrm{Q}}|$ (m).

### C. Apparent electrical impedance

We now consider a tetrapolar electrical impedance measurement (Figure 2). The source (+) and sink (−) current electrodes are $S_+$ and $S_-$, respectively; and the differential voltage is measured between high (+) and low (−) potential electrodes $E_+$ and $E_-$, respectively. The measured potential difference $\Delta V \in \mathbb{C}$ (V) is defined as

$$\Delta V := \left(\widetilde{U}^{(1)}_{++} - \widetilde{U}^{(1)}_{+-}\right) - \left(\widetilde{U}^{(1)}_{-+} - \widetilde{U}^{(1)}_{--}\right), \tag{8}$$

where $\widetilde{U}^{(1)}_{++}$ and $\widetilde{U}^{(1)}_{+-}$ are the first order approximation of the electrical potential from from (7) generated by a current source electrode $S_+$ and recorded by the high potential $E_+$ and low potential $E_-$ electrode, respectively; $\widetilde{U}^{(1)}_{-+}$ and $\widetilde{U}^{(1)}_{--}$ are the first order approximation of the electrical potential generated by a current source electrode $S_-$ and recorded by the high potential $E_+$ and low potential $E_-$ electrode, respectively. Substituting (7) into (8) gives the measured potential difference

$$\Delta V = \frac{I}{2\pi\gamma_1}\left(G + 2K\Gamma\right), \tag{9}$$

where $K := K^{++}_{\Omega_2} - K^{+-}_{\Omega_2} + K^{--}_{\Omega_2} - K^{-+}_{\Omega_2}$, $G := \frac{1}{R_{++}} - \frac{1}{R_{+-}} + \frac{1}{R_{--}} - \frac{1}{R_{-+}}$, and

$$K^{mn}_{\Omega_2} := -\frac{1}{2\pi}\iint_{\partial\Omega_2} \frac{\partial R_{\mathrm{QS}_m}(\mathbf{r}_{\mathrm{Q}})}{\partial \mathbf{n}} \cdot \mathbf{n} \frac{\mathrm{d}\left(\partial\Omega_2\right)}{R^2_{\mathrm{QS}_n}(\mathbf{r}_{\mathrm{Q}}) R_{\mathrm{QE}_m}(\mathbf{r}_{\mathrm{Q}})}$$

with $m,n \in \{+,-\}$ are geometrical constants ($\mathrm{m}^{-1}$) determined by the position of the current and voltage electrodes and the shape and position of domain $\Omega_2$, $R_{\mathrm{QS}_n}$, $R_{\mathrm{QE}_m}$ are the distances between $Q$ and the electrodes $S_n$, $E_m$, respectively; $R_{mn}$ is the distance between electrodes $S_n$ and $E_m$. Finally, the apparent electrical impedance $Z \in \mathbb{C}$ ($\Omega$) from (9) is

$$Z := R + jX = \frac{\Delta V}{I} = \frac{1}{2\pi\gamma_1}\left(G + 2K\Gamma\right), \tag{10}$$

where $R, X \in \mathbb{R}$ are the apparent resistance and reactance, respectively, and the phase is defined as $P := \tan^{-1}(X/R)$ (rad).

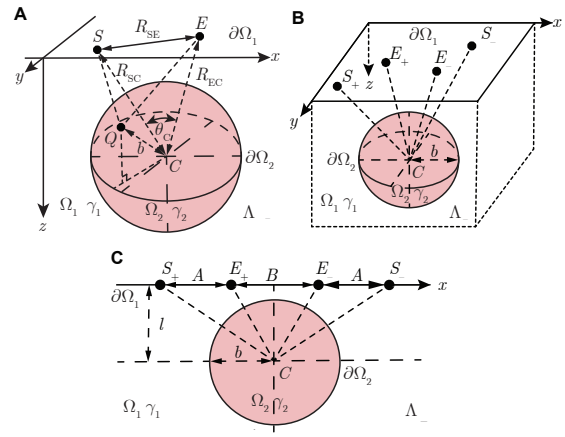


Fig. 3. Case study of a nonhomogenous model $\Lambda_-$ including tissue $\Omega_1$ and spherical volume $\Omega_2$. The admittivity and boundary of $\Omega_1$ and $\Omega_2$ are $\gamma_1$ and $\partial\Omega_1$ and $\gamma_2$ and $\partial\Omega_2$, respectively. The domain $\Omega_2$ is centered at $C$ and has radius $b$. A source of electrical current $S$ located at $\mathbf{r}_{\mathrm{S}} := (x_{\mathrm{S}}, y_{\mathrm{S}}, 0)$ on $\partial\Omega_1$ generates electrical current within the model. The recording electrode $E$ with coordinates $\mathbf{r}_{\mathrm{E}} := (x_{\mathrm{E}}, y_{\mathrm{E}}, 0)$ is located on $\partial\Omega_1$ where we want to determine the electrical potential. The an arbitrary point $Q$ with coordinates $\mathbf{r}_{\mathrm{Q}} := (x_{\mathrm{Q}}, y_{\mathrm{Q}}, z_{\mathrm{Q}})$ is located on $\partial\Omega_2$ and $\mathbf{n}$ is the outward normal vector at $Q$. $R_{\mathrm{SE}}$ is the distance between $S$ and $E$; $R_{\mathrm{SC}}$ is the distance between $S$ and $C$; $R_{\mathrm{EC}}$ is the distance between $E$ and $C$; $\theta_{\mathrm{C}}$ is the angle between the line segment $|SC|$ and $|EC|$. (B) Schematic illustrating a tetrapolar electrical impedance measurement on $\partial\Omega_1$. The current source (+) and sink (−) electrodes are $S_\pm$ and the high (+) and low (−) voltage measuring electrodes are $E_\pm$ placed on $\partial\Omega_1$. (C) Tetrapolar electrical impedance measurement with linearly aligned current source electrodes $S_\pm$ and measuring voltage $E_\pm$ electrodes. The spherical center $C$ satisfies $|CS_+| = |CS_-|$. The distance from $C$ to line segment $|E_+E_-|$ is $l$. The distance between current and voltage electrodes is $A$, whereas the distance between voltage electrodes is $B$.

### D. Apparent electrical impedance sensitivity

To determine needle EIM sensitivity to changes in tissues' electrical properties, we include a "small" change of admittivity $\gamma + \Delta\gamma$ in (10). Then, the apparent electrical impedance sensitivity $\Delta Z/Z$ to changes in tissue admittivity $|\Delta\gamma| \ll |\gamma|$ with $\Delta\gamma := \Delta\sigma + j\omega\Delta\varepsilon$, can be approximated using the 1st-order Taylor expansion as follows

$$\frac{\Delta Z_1}{Z} \approx -\frac{\Delta\gamma_1}{\gamma_1}\left(1 - \frac{2\varpi}{Z}\right) \quad \text{and} \quad \frac{\Delta Z_2}{Z} \approx -\frac{\Delta\gamma_2}{\gamma_2}\frac{2\varpi}{Z}, \tag{11}$$

where $\varpi := K\gamma_2/\left(\pi(\gamma_1+\gamma_2)^2\right)$ ($\Omega$).

### E. Case study 1: spherical volume

Here, we derive an analytical impedance expression for the special case when $\Omega_2$ can be considered as a spherical volume (see Figure 3A). According to Lemma 1 in the Supplementary Information, the first order approximation of the electrical potential distribution $\widetilde{U}^{(1)}(\mathbf{r}_{\mathrm{E}})$ recorded on $\partial\Omega_1$ can be expressed using (7), where now

$$K_{\Omega_2} = \frac{1}{b}\sum_{n=0}^{\infty}\frac{2n}{2n+1}\left(\frac{b^2}{R_{\mathrm{SC}}R_{\mathrm{EC}}}\right)^{n+1} P_n(\cos\theta_{\mathrm{C}}), \tag{12}$$

where $\theta_{\mathrm{C}}$ is the angle between line segment $\|SC\|$ and line segment $\|EC\|$, $\cos\theta_{\mathrm{C}} = (R^2_{\mathrm{SC}} + R^2_{\mathrm{EC}} - R^2_{\mathrm{SE}})/(2R_{\mathrm{SC}}R_{\mathrm{EC}})$; $b$ is the radius of $\Omega_2$; $R_{\mathrm{SC}}$ is the distance between $S$ and $C$; $R_{\mathrm{EC}}$ is the distance between $E$ and $C$; $R_{\mathrm{SE}}$ is the distance between $S$ and $E$; and $P_n(x)$ is a Legendre polynomial of degree $n$.

The electrical potential difference, apparent electrical impedance measured and apparent impedance sensitivity can be evaluated using (9), (10) and (11) in which now

$$K = \sum_{n=0}^{\infty} G_n, \tag{13}$$

where

$$G_n := \frac{2nb^{2n+1}}{2n+1} \cdot \left( \frac{P_n(\cos\theta_{++})}{R_{\mathrm{CS}_+}^{n+1} R_{\mathrm{CE}_+}^{n+1}} - \frac{P_n(\cos\theta_{+-})}{R_{\mathrm{CS}_-}^{n+1} R_{\mathrm{CE}_+}^{n+1}} + \frac{P_n(\cos\theta_{--})}{R_{\mathrm{CS}_-}^{n+1} R_{\mathrm{CE}_-}^{n+1}} - \frac{P_n(\cos\theta_{-+})}{R_{\mathrm{CS}_+}^{n+1} R_{\mathrm{CE}_-}^{n+1}} \right);$$

$\theta_{mn}$ is the angle between line segment $|CS_m|$ and $|CE_n|$ where $m,n \in \{+,-\}$, $R_{\mathrm{CS}_+}$, $R_{\mathrm{CS}_-}$, $R_{\mathrm{CE}_+}$, $R_{\mathrm{CE}_-}$ are the distances between $C$ and the electrodes $S_+$, $S_-$, $E_+$, $E_-$, respectively. If the current source and voltage recording electrodes are linearly aligned on $\partial\Omega_1$ and $|CS_+| = |CS_-|$ (Figure 3C), then

$$G = \frac{2B}{A(A+B)}, \tag{14}$$

and $G_n$ in (13) is

$$G_n = \frac{4nb^{2n+1}}{2n+1} \left(\frac{4}{L}\right)^{n+1} \left( P_n\left(\frac{4l^2+t}{L}\right) - P_n\left(\frac{4l^2-t}{L}\right) \right),$$

with $G_0 = 0$ and where $L := \sqrt{(2A+B)^2+4l^2}\sqrt{B^2+4l^2}$, $t := 2AB+B^2$, the distance between current and voltage electrodes is $A$ whereas the distance between voltage electrodes is $B$; $l$ is the distance between the center of the sphere $C$ and the center of line segment $|E_+E_-|$.

### F. Case study 2: two-layered tissue

Consider a two-layered tissue such as subcutaneous fat tissue overlying skeletal muscle tissue, i.e., $\Omega_2 : z > h_1$ has a curvature $\partial\Omega_2$ that is 0 (Figure 4A), and $h_1$ is the thickness of tissue $\Omega_1$. According to Lemma 2 in the Supplementary Information, the first order approximation of the electrical potential distribution $\widetilde{U}^{(1)}(\mathbf{r}_{\mathrm{E}})$ on $\partial\Omega_1$ can be expressed using (7), in which now

$$K_{\Omega_2} = \frac{1}{\sqrt{R_{\mathrm{SE}}^2 + 4h_1^2}}, \tag{15}$$

where $R_{\mathrm{SE}}$ is the distance between $S$ and $E$.

In this case, the recorded electrical potential difference, apparent electrical impedance and apparent impedance sensitivity in Figure 4B can be evaluated by (9), (10) and (11) in which

$$\begin{aligned} K = &\frac{1}{\sqrt{R_{S_+E_+}^2 + 4h_1^2}} - \frac{1}{\sqrt{R_{S_-E_+}^2 + 4h_1^2}} \\ &+ \frac{1}{\sqrt{R_{S_-E_-}^2 + 4h_1^2}} - \frac{1}{\sqrt{R_{S_+E_-}^2 + 4h_1^2}}, \end{aligned} \tag{16}$$

where $R_{mn}$ is the distance between $m = \in \{S_+, S_-\}$ and $n = \in \{E_+, E_-\}$. When the four electrodes are linearly aligned (see Figure 4C), the geometric constant simplifies to

$$K = \frac{2}{\sqrt{A^2+4h_1^2}} - \frac{2}{\sqrt{(A+B)^2+4h_1^2}}$$

and $G$ equals (14).

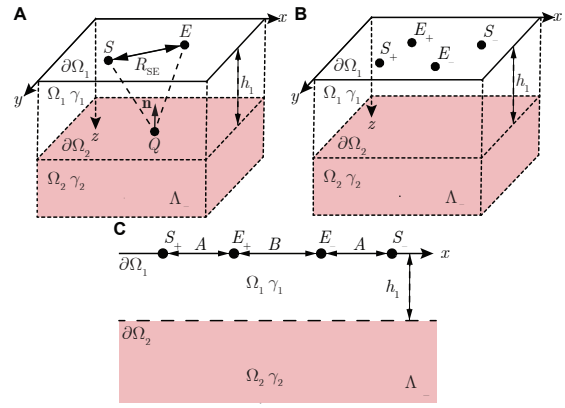


Fig. 4. Case study of a nonhomogeneous model $\Lambda_-$ consistinvg of a two-layered tissue. The admittivity and boundary of domains $\Omega_1$ and $\Omega_2$ are $\gamma_1$ and the parallel plane $\partial\Omega_1$ and $\gamma_2$ and the parallel plane $\partial\Omega_2$, respectively. The thickness of $\Omega_1$ is $h_1$. A source $S$ with coordinates $\mathbf{r}_{\mathrm{S}} := (x_{\mathrm{S}}, y_{\mathrm{S}}, 0)$ on $\partial\Omega_1$ applies electrical current into the model. The electrode $E$ with coordinates $\mathbf{r}_{\mathrm{E}} := (x_{\mathrm{E}}, y_{\mathrm{E}}, 0)$ is an arbitrary point on $\partial\Omega_1$ where we want to determine the electrical potential. The position $Q$ with coordinates $\mathbf{r}_{\mathrm{Q}} := (x_{\mathrm{Q}}, y_{\mathrm{Q}}, h_1)$ is an arbitrary point on $\partial\Omega_2$ and $\mathbf{n}$ is the outward normal vector at $Q$. $R_{\mathrm{SE}}$ is the distance between $S$ and $E$. (B) Schematic illustrating a tetrapolar electrical impedance measurement on $\partial\Omega_1$. The current source (+) and sink (−) electrodes are $S_\pm$ and the high (+) and low (−) voltage measuring electrodes are $E_\pm$ placed on $\partial\Omega_1$. (C) Tetrapolar electrical impedance measurement with linearly aligned current source electrodes $S_\pm$ and measuring voltage $E_\pm$ electrodes. The distance between current and voltage electrodes is $A$, whereas the distance between voltage electrodes is $B$.

## III. Bidomain tissue model in full space

### A. Governing equation

We extend the previous framework in full space $\Lambda \in \mathbb{R}^3$. The new model (denoted by the superscript $'$) contains domains $\Omega_1'$ and $\Omega_2$ where $\Lambda := \Omega_1' \cup \Omega_2$ and $\Omega_1' \cap \Omega_2 = \partial\Omega_2$. In this full space model, we consider an electrical current source $S'$ located at arbitrary position $\mathbf{r}_{\mathrm{S}'} := (x_{\mathrm{S}'}, y_{\mathrm{S}'}, z_{\mathrm{S}'})$ in $\Omega_1'$. Since $\Omega_1'$ has now no boundary conditions, the governing equation of $U'(\mathbf{r})$ is (3) in which $\mathbf{r}_{\mathrm{S}}$ is replaced with $\mathbf{r}_{\mathrm{S}'}$.

### B. Electric potential distribution

In full space, the image term in (5) disappears and the $p$th-order electrical potential approximation $\widetilde{U}'^{(p)}(\mathbf{r})$ is

$$\begin{cases} \widetilde{U}'^{(p)}(\mathbf{r}) &:= \frac{I}{4\pi\gamma_1 |\mathbf{r}-\mathbf{r}_{\mathrm{S}'}|} + \widetilde{U}_{\Omega_2}'^{(p)}(\mathbf{r}) \\ \widetilde{U}'^{(0)}(\mathbf{r}) &:= \frac{I}{4\pi\gamma_1 |\mathbf{r}-\mathbf{r}_{\mathrm{S}'}|} \\ \widetilde{U}_{\Omega_2}'^{(p)}(\mathbf{r}) &:= \frac{\Gamma_2}{2\pi} \iint_{\partial\Omega_2} \frac{\partial \widetilde{U}'^{(p-1)}(\mathbf{r}_{\mathrm{Q}})}{\partial \mathbf{n}} \cdot \mathbf{n} \frac{\mathrm{d}(\partial\Omega_2)}{|\mathbf{r}-\mathbf{r}_{\mathrm{Q}}|}, \end{cases} \tag{17}$$

where $\mathbf{r} \in \Lambda - \mathbf{r}_{\mathrm{S}'}$ and $U' = \lim_{p\to\infty} \widetilde{U}'^{(p)}$.

### C. Apparent electrical impedance

The electrical potential is recording via voltage measuring electrode $E'$ at $\mathbf{r}_{\mathrm{E}'} := (x_{\mathrm{E}'}, y_{\mathrm{E}'}, z_{\mathrm{E}'})$ in $\Omega_1'$. According to (17), the first order approximated electrical potential recorded is

$$\widetilde{U}'^{(1)}(\mathbf{r}_{\mathrm{E}'}) = \frac{I}{4\pi\gamma_1} \left( \frac{1}{R_{\mathrm{S}'\mathrm{E}'}} + K_{\Omega_2}'\Gamma \right), \tag{18}$$

where $R_{\mathrm{S}'\mathrm{E}'}$ is the distance between electrodes $S'$ and $E'$, $K_{\Omega_2}'$ maintains the same definition as $K_{\Omega_2}$ in (7) replacing $S$, $E$ with $S'$, $E'$.

TABLE I
FINITE ELEMENT MODEL SIMULATION SETTINGS.

| Parameters | | Half space $\Lambda_-$ | | Full space $\Lambda$ | |
|---|---|---|---|---|---|
| Symbol | Unit | Spherical volume | Two-layered tissue | Spherical volume | Two-layered tissue |
| $I$ | mA | 1 | 1 | 1 | 1 |
| $\omega\cdot(2\pi)^{-1}$ | kHz | 50 | 50 | 50 | 50 |
| $A$ | mm | 3 | 3 | 3 | 3 |
| $B$ | mm | 8 | 8 | 8 | 8 |
| $l$ | mm | [5,15] | - | [5,15] | - |
| $b$ | mm | [1,6] | - | [1,6] | - |
| $h_1$ | mm | - | [2,22] | - | [2,22] |
| $\sigma_1$ | S m$^{-1}$ | $\sigma_m$ | $\sigma_m$ | $\sigma_m$ | $\sigma_m$ |
| $\sigma_2$ | S m$^{-1}$ | $[0.5, 1.5]\sigma_m$ | $[0.5, 1.5]\sigma_m$ | $[0.5, 1.5]\sigma_m$ | $[0.5, 1.5]\sigma_m$ |
| $\varepsilon_{r1}$ | - | $\varepsilon_m$ | $\varepsilon_m$ | $\varepsilon_m$ | $\varepsilon_m$ |
| $\varepsilon_{r2}$ | - | $[0.5, 1.5]\varepsilon_m$ | $[0.5, 1.5]\varepsilon_m$ | $[0.5, 1.5]\varepsilon_m$ | $[0.5, 1.5]\varepsilon_m$ |

For impedance measurement, the source (+) and sink (−) current electrodes are $S'_+$ and $S'_-$ respectively; and the voltage drop is measured between high (+) and low (−) potential electrodes $E'_+$ and $E'_-$, respectively. From (8), (10) and (18), the apparent electrical impedance is

$$Z' = \frac{1}{4\pi\gamma_1}\left(G' + K'\Gamma\right), \tag{19}$$

where $K'$ maintains the same definition as $K$ in (9) replacing $S$, $E$ with $S'$, $E'$; $G' := \frac{1}{R'_{++}} - \frac{1}{R'_{+-}} + \frac{1}{R'_{--}} - \frac{1}{R'_{-+}}$; $R'_{mn}$ is the distance between electrode $S'_m$ and $E'_n$ with $m,n =\in \{+,-\}$.

### D. Apparent electrical impedance sensitivity

Following the same rationale as in Section II-D, the impedance sensitivity expressions to changes in admittivity in $\Omega'_1$ and $\Omega_2$ are, respectively,

$$\frac{\Delta Z'_1}{Z'} \approx -\frac{\Delta\gamma_1}{\gamma_1}\left(1 - \frac{\varpi'}{2Z'}\right) \quad \text{and} \quad \frac{\Delta Z'_2}{Z'} \approx -\frac{\Delta\gamma_2}{\gamma_2}\frac{\varpi'}{2Z'}. \tag{20}$$

where $\varpi'$ maintains the same definition as $\varpi$ in (11) replacing $K$ with $K'$.

## IV. MATERIALS AND METHODS

### A. Finite element model electrostatic simulations

For our isotropic finite element model (FEM) simulations (Comsol Multiphysics, Comsol, Inc., Burlington, MA, USA), we calculated the geometric mean muscle conductivity $\sigma_m = 0.47$ S m$^{-1}$ and relative permittivity $\varepsilon_m = 6.7\times10^3$ (dimensionless) from the longitudinal and transverse anisotropic muscle conductivity and relative permittivity values at 50 kHz available in [15]. The model parameters $\sigma_2$, $\varepsilon_{r2}$, $l$, $h_1$ and $b$ are simulation variables. For the spherical volume simulations, the domains $\Omega_1$ and $\Omega'_1$ are modeled as cuboids with dimensions width × length × height $140\times140\times100$ mm and $140\times140\times200$ mm, respectively. For the two-layered tissue simulations, $\Omega_2$ is modeled as a cuboid with dimensions $140\times140\times(100-h_1)$ mm, whereas $\Omega_1$ and $\Omega'_1$ have dimensions $140\times140\times h_1$ mm and $140\times140\times(100+h_1)$ mm, respectively. Adaptive mesh is utilized where the minimum mesh element size is $10^{-4}$ mm, the maximum element growth rate is 1.2 and the curvature factor is 0.2. The total elements for the spherical volume model in half and full space are 351,675 are 667,763 respectively; and for the two-layered model these are 307,041 and 640,121 in half and full space, respectively.

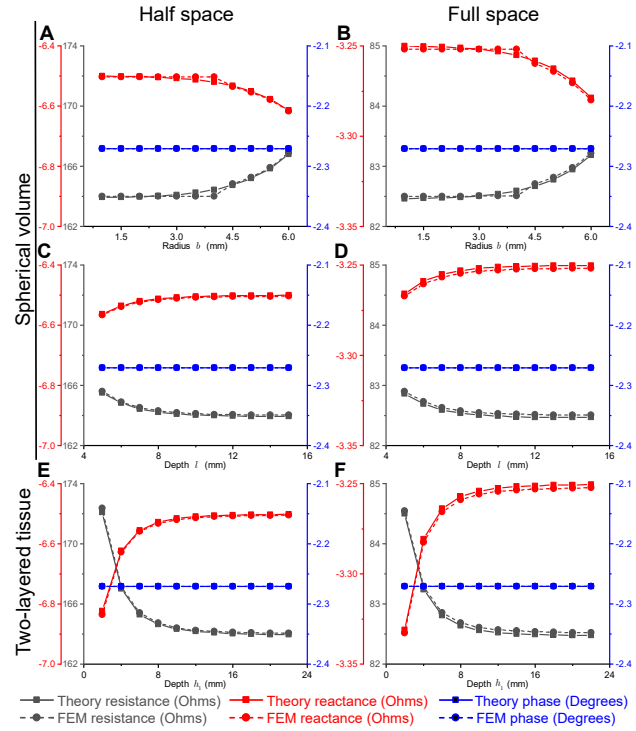


Fig. 5. Comparison of the electrical resistance, reactance and phase results between theory (solid line) and finite element model (FEM, dotted line). Spherical intrusion in half (A) and full (B) space changing the sphere radius $b = [1,6]$ mm and constant depth $l = 7$ mm. Spherical intrusion in half (C) and full (D) space changing the depth $l = [5,15]$ mm and constant radius $b = 4$ mm. Two-layered model in half (E) and full (F) space with thickness $h_1 = [4,22]$ mm. Simulation setting parameters are $\sigma_2 = 0.9\sigma_m$, $\varepsilon_{r2} = 0.9\varepsilon_m$.

### B. Numerical electrical impedance

The impedance is computed in MATLAB (The Mathworks, Natick, MA, USA) using (10) and (19). To evaluate the accuracy of our theoretical predictions, we define the conductivity and permittivity (relative) difference as $\delta_\sigma := (\sigma_2 - \sigma_1)/\sigma_1$ and $\delta_\varepsilon := (\varepsilon_2 - \varepsilon_1)/\varepsilon_1$, respectively. Finally, the resistance, reactance and phase error between the theoretical and FEM simulated impedance are calculated as $e_R := (R_{\text{Theory}} - R_{\text{FEM}})/R_{\text{FEM}}$, $e_X := (X_{\text{Theory}} - X_{\text{FEM}})/X_{\text{FEM}}$ and $e_P := (P_{\text{Theory}} - P_{\text{FEM}})/P_{\text{FEM}}$, respectively.

## V. SIMULATION RESULTS

Figure 5 compares the impedance obtained with our theoretical framework and that obtained via FEM simulations. For the spherical simulations, data similarity increases when the dimension (Figure 5 A and B) and depth (Figure 5 C and D) of the spherical volume decreases and increases, respectively. The similarity for the two-layered tissue model is in good agreement varying the tissue thickness (Figure 5 E and F). Of note, both theory and FEM results reflects that the phase of impedance is not sensitive to geometric changes. This was expected as the phase it is calculated as the ratio between reactance and resistance and thus these effects are canceled.

Figure 6 plots the accuracy of the first order apparent impedance predictions compared to FEM simulation varying the conductivity and relative permittivity properties of the tissues from -50% to 50% while keeping the rest of simulation

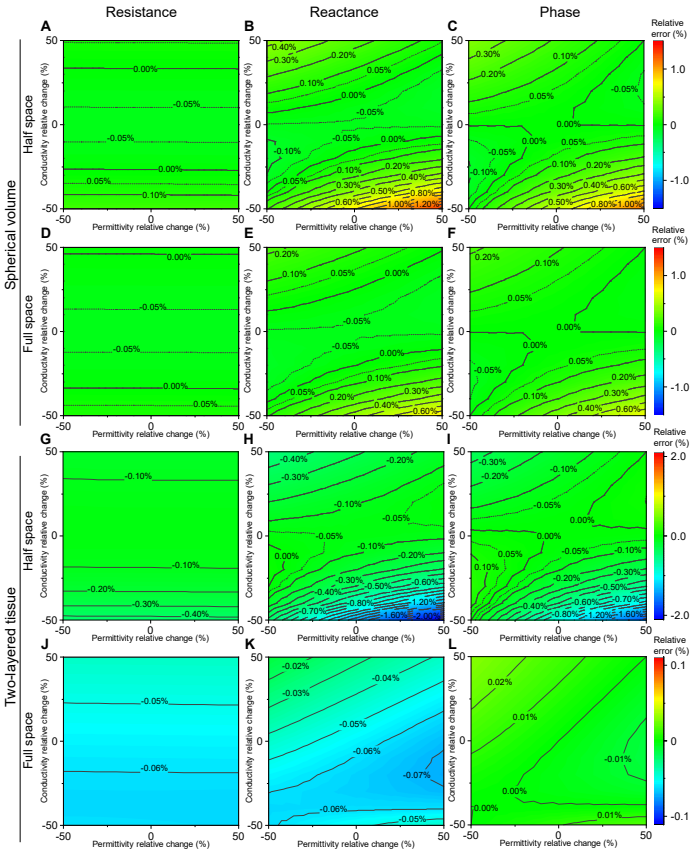


Fig. 6. Relative resistance, reactance and phase error plots as function of the admittivity differences in the spherical volume model in half (A, B, C) and full (D, E, F) space, and the two-layered tissue model in half (G, H, I) and full (J, K, L) space. Simulation setting parameters: $l$=6 mm, $b$=4 mm and $h_1$=6 mm.

parameters constant. The relative errors for the resistance, reactance and phase in the spherical volume model are $\leq$0.2%, $\leq$1.2% and $\leq$1.0%. For the two-layered tissue model, the relative errors are $\leq$2%. Overall, the two-layered cases have larger errors than corresponding spherical cases, the reactance errors have the largest errors comparing with resistance and phase errors, while the half space model has larger errors than corresponding full space model.

## VI. Discussion

This paper describes a physics-driven framework to model needle EIM measurements considering a nonhomogeneous and isotropic half- and full-space bidomain tissue model. In addition, we performed an impedance sensitivity analysis to determine the sensitivity of needle EIM to changes occurring in the electrical properties within the model. Practically, this knowledge can be useful to inform the design and placement of electrodes for "sensitive" needle EIM measurements of muscle. We also provided compact and simple analytical expressions for two particular case studies. Finally, we confirmed the usefulness of our theoretical framework performing a head-to-head numerical and FEM comparison.

Our results shows reactance gave similar relative errors as the phase but larger than the resistance (Figure 6). One possible explanation is because reactance and phase absolute values are much smaller than their resistance counterpart and therefore the discrepancies are magnified when calculating the relative errors. Subsequently, relative errors tend to increase when absolute differences and values are small as it is the case for the reactance. Still, overall the relative errors between the framework and FEM simulations are in good agreement with maximum relative errors that are $\leq$2%.

This work extends our initial (pre-)clinical studies applying needle EIM [3], [8], [9] by developing a framework capable of modeling the impact of muscle inhomogeneities. Our ongoing efforts are focused on establishing the background and the development of needle EIM to ensure future evaluation of this technology in the clinical practice. We foresee the value of measuring EIM and EMG directly in the muscle using needles helping to expand our understanding of the relationships between the impedimetric and electromyographic properties of muscle in health and disease. For example, we anticipate that motor unit potential (MUP) alterations that occur in chronic neurogenic disease (such as increased duration and amplitude of the MUPs) will be associated with needle EIM features of reinnervation/type grouping, including increasing change in resistance and reactance values.

This study has limitations. First, we restricted ourselves to study a bidomain model, in which the admittivity properties are considered to be isotropic. Further work is necessary to extend our results to a more general multi-domain model with anisotropic electrical properties. In the half-space case, the source and electrodes are assumed to be positioned on a planar surface. In practice, the electrodes might be placed on a more complex surface, for example, affected by the curvature of a limb [24]. In the full-space case, electrodes can only be placed in one domain: our framework can not describe the case with current and voltages electrodes are placed in domains with different admittivity property or even placed on the boundary between tissues. In addition to this, in a bidomain model, there is only one heterogeneity possible, where the two domains that form the model form a "*series*"-like equivalent electrical circuit –in other words, the current has to flow through one domain before flowing into the second domain–. Further research is warranted to extend our work and develop a multi-domain, anisotropic framework for modeling EIM readings considering different types tissue inhomogeneities. Future work will include experimental validation performing needle EIM measurements on phantom media with known electrical properties and measuring patients using ultrasound as a reference.

## VII. Conclusions

This study proposes a novel framework to model EIM readings in nonhomogeneous muscle considering a bidomain model. The validity of our methodology has been tested against FEM simulations. We believe this knowledge may lead to new ways for interpreting EIM in diseased muscle causing changes in muscle composition, a common feature in many neuromuscular disorders, therefore, having a direct impact on its clinical application.

## REFERENCES


[1] M. Noshiro, T. Morimoto, H. Nagao, and H. Matsuda, "Electrical impedance in the lower limbs of patients with Duchenne muscular dystrophy: A preliminary study," *Medical & Biological Engineering & Computing*, vol. 31, no. 2, pp. 97–102, mar 1993.

[2] B. Sanchez, O. G. Martinsen, T. J. Freeborn, and C. M. Furse, "Electrical impedance myography: A critical review and outlook," *Clinical Neurophysiology*, vol. 132, no. 2, pp. 338–344, feb 2021.

[3] H. Kwon, S. B. Rutkove, and B. Sanchez, "Recording characteristics of electrical impedance myography needle electrodes," *Physiological Measurement*, vol. 38, no. 9, pp. 1748–1765, aug 2017.

[4] L. K. Huang, L. N. Huang, Y. M. Gao, Z. Lucev Vasic, M. Cifrek, and M. Du, "Electrical Impedance Myography Applied to Monitoring of Muscle Fatigue During Dynamic Contractions," *IEEE Access*, vol. 8, pp. 13 056–13 065, 2020.

[5] J. J. Alix, H. E. McDonough, B. Sonbas, S. J. French, D. G. Rao, V. Kadirkamanathan, C. J. McDermott, T. J. Healey, and P. J. Shaw, "Multi-dimensional electrical impedance myography of the tongue as a potential biomarker for amyotrophic lateral sclerosis," *Clinical Neurophysiology*, vol. 131, no. 4, pp. 799–808, apr 2020.

[6] D. Li, L. Huang, Y. Wen, Y. Gao, Z. L. Vasic, M. Cifrek, and M. Du, "Analysis of Electrical Impedance Myography Electrodes Configuration for Local Muscle Fatigue Evaluation Based on Finite Element Method," *IEEE Access*, vol. 8, pp. 172 233–172 243, 2020.

[7] J. A. Nagy, C. J. DiDonato, S. B. Rutkove, and B. Sanchez, "Permittivity of ex vivo healthy and diseased murine skeletal muscle from 10 kHz to 1 MHz," *Nature Scientific Data*, vol. 6, no. 1, p. 37, dec 2019.

[8] H. Kwon, J. F. Di Cristina, S. B. Rutkove, and B. Sanchez, "Recording characteristics of electrical impedance-electromyography needle electrodes," *Physiological Measurement*, vol. 39, no. 5, p. 055005, may 2018.

[9] M. Martinez de Morentin Cardoner, H. Kwon, H. V. Gutierrez Pulido, J. A. Nagy, S. B. Rutkove, and B. Sanchez, "Modeling and reproducibility of twin concentric electrical impedance myography," *IEEE Transactions on Biomedical Engineering*, p. in press, 2021.

[10] J. Kimura, "Long and short of nerve conduction measures: Reproducibility for sequential assessments," *Journal of Neurology, Neurosurgery and Psychiatry*, vol. 71, no. 4, pp. 427–430, oct 2001.

[11] D. S. Pinheiro, G. M. Manzano, and J. A. M. Nóbrega, "Reproducibility in nerve conduction studies and F-wave analysis," *Clinical Neurophysiology*, vol. 119, no. 9, pp. 2070–2073, sep 2008.

[12] M. B. Offit, T. Wu, M. K. Floeter, and T. J. Lehky, "Electrical impedance myography (EIM) in a natural history study of C9ORF72 mutation carriers," *Amyotrophic Lateral Sclerosis and Frontotemporal Degeneration*, vol. 21, no. 5-6, pp. 445–451, jul 2020.

[13] K. Kapur, B. Sanchez, A. Pacheck, B. Darras, S. B. Rutkove, and R. Selukar, "Functional Mixed-Effects Modeling of Longitudinal Duchenne Muscular Dystrophy Electrical Impedance Myography Data Using State-Space Approach," *IEEE Transactions on Biomedical Engineering*, vol. 66, no. 6, pp. 1761–1768, jun 2019.

[14] J. Hamel, P. Lee, M. D. Glenn, T. Burka, I. Choi, S. D. Friedman, D. W. W. Shaw, A. McCalley, L. Herbelin, M. M. Dimachkie, R. Lemmers, S. M. Maarel, R. J. Barohn, R. Tawil, and J. M. Statland, "Magnetic resonance imaging correlates with electrical impedance myography in facioscapulohumeral muscular dystrophy," *Muscle & Nerve*, vol. 61, no. 5, pp. 644–649, may 2020.

[15] D. Andreuccetti, R. Fossi, and C. Petrucci, "An Internet resource for the calculation of the dielectric properties of body tissues in the frequency range 10 Hz - 100 GHz. Based on data published by C.Gabriel et al. in 1996. [Online]. Available: http://niremf.ifac.cnr.it/tissprop/," 1997.

[16] J. W. Clark and R. Plonsey, "A mathematical study of nerve fiber interaction." *Biophysical journal*, vol. 10, no. 10, pp. 937–57, oct 1970.

[17] K. Altman and R. Plonsey, "Point source nerve bundle stimulation: effects of fiber diameter and depth on simulated excitation," *IEEE Transactions on Biomedical Engineering*, vol. 37, no. 7, pp. 688–698, jul 1990.

[18] K. W. Altman and R. Plonsey, "Analysis of the longitudinal and radial resistivity measurements of the nerve trunk," *Annals of Biomedical Engineering*, vol. 17, no. 4, pp. 313–324, jul 1989.

[19] H. Kwon, W. Q. Malik, S. B. Rutkove, and B. Sanchez, "Separation of subcutaneous fat from muscle in surface electrical impedance myography measurements using model component analysis," *IEEE Transactions on Biomedical Engineering*, vol. 66, no. 2, pp. 354–364, 2019.

[20] J. C. Maxwell, *Electricity and magnetism*, Oxford, 1892.

[21] P. N. Robillard and D. Poussart, "Spatial resolution of four electrode array." *IEEE transactions on bio-medical engineering*, vol. 26, no. 8, pp. 465–70, aug 1979.

[22] H. S. Cohl and J. E. Tohline, "A Compact Cylindrical Green's Function Expansion for the Solution of Potential Problems," *The Astrophysical Journal*, vol. 527, no. 1, pp. 86–101, dec 1999.

[23] A.-M. Wazwaz, "The variational iteration method: A reliable analytic tool for solving linear and nonlinear wave equations," *Computers & Mathematics with Applications*, vol. 54, no. 7-8, pp. 926–932, oct 2007.

[24] B. Sanchez, A. Pacheck, and S. B. Rutkove, "Guidelines to electrode positioning for human and animal electrical impedance myography research," *Scientific Reports*, vol. 6, no. 1, p. 32615, dec 2016.


## ACKNOWLEDGMENT

This work was funded by the China Scholarship Council grant 201906020024 (XL) and National Institutes of Health grant R41 NS112029-01A1 (BS).

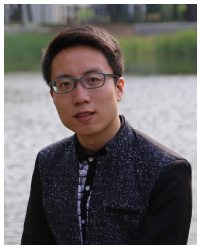

**Xuesong Luo** received a B.S. degree in Electrical Engineering from Beihang University, China in 2016. Since 2016, he is pursuing a Ph.D. degree in Electromechanical Engineering in Beihang University. From February 2018 to June 2018, he was a visiting student in Department of Transport in Cranfield University, Bedford, UK. From 2019-2020, he was a visiting P.hD. student in the Department of Neurology, Beth Israel Deaconess Medical Center–Harvard Medical School, Boston, USA. Since September 2020, he has been a visiting P.hD. student in the Department of Electrical and Computer Engineering, University of Utah, Salt Lake City, USA. His main interests are health management and bioimpedance measurement.

**Shaoping Wang** received a B.S., M.S. and Ph.D. degrees in mechanical engineering from Beihang University, Beijing, China in 1988, 1991 and 1994, respectively. She is a professor in the Department of Automation Science and Electrical Engineering, Beihang University. She has more than 20 years of experience in academic teaching and research in fault diagnosis and system reliability. She has published more than 200 technical papers and three major textbooks. Her major research interests include fault diagnosis, system reliability, health management and biomedical monitoring.

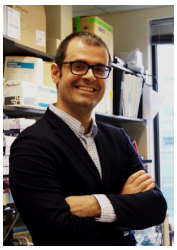

**Benjamin Sanchez Terrones** (M'13-SM'20), received a dual B.S. degree in Telecommunication and Electronic Engineering, and the M.S, and Ph.D. degrees in Electronic Engineering from Universitat Politecnica de Catalunya (UPC), Barcelona, Spain, in 2006, 2007, 2008, and 2012, respectively.

He was a Visiting Scholar in the Department of Fundamental Electricity and Instrumentation, Vrije Universiteit Brussel, Brussels, Belgium, and the Department of Automatic Control, School of Electrical Engineering, Royal Institute of Technology (KTH), Stockholm, Sweden, in 2012 and 2013, respectively. From 2014−2020, he was Instructor in Neurology at Beth Israel Deaconess Medical Center, Harvard Medical School, Boston, MA, USA. Since 2020, he has been an Assistant Professor of Electrical and Computer Engineering at the University of Utah and Member of the Huntsman Cancer Center, Salt Lake City, UT, USA. His research focuses on developing novel bioimpedance technologies for measuring and monitoring health.

Dr. Sanchez has co-authored 67 articles published in refereed international physics, medicine and engineering journals, 1 book chapter, and has 4 issued and 2 pending patents. His research has been Highlighted by the journals Measurement Science & Technology in 2012, Physiological Measurement in 2013, 2015 and 2017, and Clinical Neurophysiology in 2020 and 2021. He was the recipient of the 2012 Ph.D. Extraordinary Prize from UPC, Martin Black prize for the Best Paper Award in Physiological Measurement journal in 2014 for his bioimpedance work, winner of the President's Research Initiative Award from the American Association of Neuromuscular & Electrodiagnostic Medicine in 2014 and 2016. Dr. Sanchez serves as Members-at-Large of the IEEE Technical Committee on Biomedical Signal Processing, and is International Advisory Board Member of Physiological Measurement journal.

# 1 Lemma 1.

If $\partial\Omega_2$ is a spherical surface centered at $C$ with radius $b$ in $\mathbb{R}^3$, $Q$ is an arbitrary point on $\partial\Omega_2$, $\mathbf{n}$ is the outward normal vector at $Q$, $S$ and $E$ are arbitrary points outside the sphere as shown in Figure A1, then

$$\begin{aligned} &-\frac{1}{2\pi}\iint_{\partial\Omega_2}\frac{\partial R_{\mathrm{SQ}}(\mathbf{r}_{\mathrm{Q}})}{\partial\mathbf{n}}\cdot\mathbf{n}\frac{\mathrm{d}\,(\partial\Omega_2)}{R_{\mathrm{SQ}}^2(\mathbf{r}_{\mathrm{Q}})R_{\mathrm{EQ}}(\mathbf{r}_{\mathrm{Q}})} \\ &=\frac{1}{b}\sum_{n=0}^{\infty}\frac{2n}{2n+1}\left(\frac{b^2}{R_{\mathrm{EC}}R_{\mathrm{SC}}}\right)^{n+1}P_n(\cos\theta_{\mathrm{C}}). \end{aligned} \tag{A1}$$

*Proof.* To calculate the surface integrals in (A1) we build an auxiliary model of charged spherical shell in vacuum that allows us to find the solution indirectly. Let's start establishing a spherical coordinates in $\mathbb{R}^3$ originated at the center $C$ of the spherical surface $\partial\Omega_2$ (see Figure A1). The position $\mathbf{r} := (r,\theta,\varphi)$ is an arbitrary defined in spherical coordinates. For convenience, we consider $S$ with coordinates $\mathbf{r}_{\mathrm{S}} := (R_{\mathrm{SC}},0,0)$ on the $z$-axis, while $E$ is defined with coordinates $\mathbf{r}_{\mathrm{E}} := (R_{\mathrm{EC}},\theta_{\mathrm{C}},0)$, while $Q$ with coordinates $\mathbf{r}_{\mathrm{Q}} := (b,\theta_{\mathrm{Q}},\varphi_{\mathrm{Q}})$ is an arbitrary point on $\partial\Omega_2$. $R_{\mathrm{SC}}$ is the distance between $S$ and $C$; $R_{\mathrm{EC}}$ is the distance between $E$ and $C$; $R_{\mathrm{SQ}}$ is the distance between $S$ and $Q$; $R_{\mathrm{EQ}}$ is the distance between $E$ and $Q$; $\theta_{\mathrm{C}}$ is the angle between line segment $|SC|$ and $|EC|$; $\theta_{\mathrm{Q}}$ is the angle between line segment $|QC|$ and $|SC|$. Next, we introduce a charge density function $q(\mathbf{r}_{\mathrm{Q}}) \in \mathbb{R}$ (C m$^{-2}$) on the spherical surface $\partial\Omega_2$, defined as

$$q(\mathbf{r}_{\mathrm{Q}}) := \frac{\partial R_{\mathrm{SQ}}(\mathbf{r}_{\mathrm{Q}})}{\partial\mathbf{n}}\cdot\mathbf{n}\frac{1}{R_{\mathrm{SQ}}^2(\mathbf{r}_{\mathrm{Q}})}.$$

Then the potential distribution $U(\mathbf{r})$ caused by $q$ can be expressed as

$$U(\mathbf{r}) = \frac{1}{4\pi\varepsilon_0}\iint_{\partial\Omega_2}\frac{\partial R_{\mathrm{SQ}}(\mathbf{r}_{\mathrm{Q}})}{\partial\mathbf{n}}\cdot\mathbf{n}\frac{1}{R_{\mathrm{SQ}}^2(\mathbf{r}_{\mathrm{Q}})}\frac{\mathrm{d}\,(\partial\Omega_2)}{|\mathbf{r}-\mathbf{r}_{\mathrm{Q}}|}. \tag{A2}$$

According to the axial symmetry, $U$ has no dependence on the azimuthal angle $\varphi$. Then applying separation of variables to Poission's equation, the general solution for potential distribution $U(\mathbf{r})$ in spherical coordinates satisfies that

$$U(\mathbf{r}) = \sum_{n=0}^{\infty}\left(A_n r^n + \frac{B_n}{r^{n+1}}\right)P_n(\cos\theta), \tag{A3}$$

where $A_n$ and $B_n$ are a series of constants and $P_n(x)$ are Legendre polynomials.

In this model, an auxiliary point $E'$ with coordinates $\mathbf{r}_{\mathrm{E}} := (R_{\mathrm{EC}},0,0)$ is introduced to solve the surface integral (A2) indirectly, which satisfy $|E'C| = |EC|$ and $E'$ is on $z$-axis. From (A3), the potential at $E'$ can be written as

$$U(\mathbf{r}_{\mathrm{E}'}) = \sum_{n=0}^{\infty}\left(A_n R_{\mathrm{EC}}^n + \frac{B_n}{R_{\mathrm{EC}}^{n+1}}\right). \tag{A4}$$

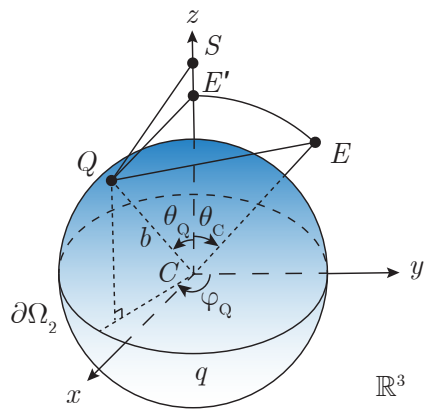


Figure A1: Auxiliary model of charged spherical shell in vacuum. A nonuniform charged spherical shell $\partial\Omega_2$ is centered at the origin of spherical coordinates $(r,\theta,\varphi)$ in infinity vacuum $\mathbb{R}^3$with $b$ the radius of $\partial\Omega_2$. The position $Q$ has coordinates $\mathbf{r}_{\mathrm{Q}} := (b,\theta_{\mathrm{Q}},\varphi_{\mathrm{Q}})$ on $\partial\Omega_2$. The charge density $q(\mathbf{r}_{\mathrm{Q}})$ is distributed on surface $\partial\Omega_2$. The position $S$, $E$ and $E'$ have coordinates $\mathbf{r}_{\mathrm{S}} := (R_{\mathrm{SC}},0,0)$, $\mathbf{r}_{\mathrm{E}} := (R_{\mathrm{EC}},\theta_{\mathrm{C}},0)$ and $\mathbf{r}_{\mathrm{E}'} := (R_{\mathrm{EC}},0,0)$ outside the sphere, which satisfy $|EC| = |E'C|$ and $S$, $E'$ are on $z$-axis. The angle $\theta_{\mathrm{C}}$ is defined between line segment $|SC|$ and $|EC|$; $\theta_{\mathrm{Q}}$ is the angle between line segment $|SC|$ and $|QC|$.

From (A2), $V(\mathbf{r}_{\mathrm{E}'})$ can also be expressed as

$$U(\mathbf{r}_{\mathrm{E}'}) = \frac{1}{4\pi\varepsilon_0}\int_{-\pi}^{\pi}\int_{0}^{\pi}\frac{\partial R_{\mathrm{SQ}}(\mathbf{r}_{\mathrm{Q}})}{\partial b}\frac{b^2\sin\theta_{\mathrm{Q}}\mathrm{d}\theta_{\mathrm{Q}}\mathrm{d}\varphi_{\mathrm{Q}}}{R_{\mathrm{SQ}}^2(\mathbf{r}_{\mathrm{Q}})R_{\mathrm{QE}'}(\mathbf{r}_{\mathrm{Q}})}, \tag{A5}$$

where

$$R_{\mathrm{SQ}}(\mathbf{r}_{\mathrm{Q}}) = \sqrt{R_{\mathrm{SC}}^2 + b^2 - 2bR_{\mathrm{SC}}\cos\theta_{\mathrm{Q}}}$$

and

$$R_{\mathrm{QE}'}(\mathbf{r}_{\mathrm{Q}}) = \sqrt{R_{\mathrm{EC}}^2 + b^2 - 2bR_{\mathrm{EC}}\cos\theta_{\mathrm{Q}}}.$$

Equation (A5) can be further simplified as

$$U(\mathbf{r}_{\mathrm{E}'}) = \frac{1}{4\varepsilon_0}\left[\frac{2b}{b^2 - R_{\mathrm{EC}}R_{\mathrm{SC}}} + \frac{1}{\sqrt{R_{\mathrm{EC}}R_{\mathrm{SC}}}}\ln\left(\frac{\sqrt{R_{\mathrm{EC}}R_{\mathrm{SC}}}+b}{\sqrt{R_{\mathrm{EC}}R_{\mathrm{SC}}}-b}\right)\right]. \tag{A6}$$

From the geometry of the model, we have that $\frac{b}{\sqrt{R_{\mathrm{EC}}R_{\mathrm{SC}}}} < 1$. According to Taylor series we have

$$\begin{cases} \ln\left(\frac{\sqrt{R_{\mathrm{EC}}R_{\mathrm{SC}}}+b}{\sqrt{R_{\mathrm{EC}}R_{\mathrm{SC}}}-b}\right) & = \sum_{n=1}^{\infty}\frac{1}{n}\frac{b^n}{R_{\mathrm{EC}}^{\frac{n}{2}}R_{\mathrm{SC}}^{\frac{n}{2}}} + \sum_{n=1}^{\infty}\frac{(-1)^{n+1}}{n}\frac{b^n}{R_{\mathrm{EC}}^{\frac{n}{2}}R_{\mathrm{SC}}^{\frac{n}{2}}} \\ \frac{2b}{b^2 - R_{\mathrm{EC}}R_{\mathrm{SC}}} & = -\frac{2b}{R_{\mathrm{EC}}R_{\mathrm{SC}}}\sum_{n=0}^{\infty}\frac{b^{2n}}{R_{\mathrm{EC}}^{n}R_{\mathrm{SC}}^{n}} \end{cases} \tag{A7}$$

Substituting (A7) into (A6) gives

$$U\left(\mathbf{r}_{\mathrm{E}'}\right)=-\frac{1}{b\varepsilon_0}\sum_{n=0}^{\infty}\frac{n}{2n+1}\left(\frac{b^2}{R_{\mathrm{EC}}R_{\mathrm{SC}}}\right)^{n+1}. \tag{A8}$$

Comparing (A8) and (A4), we have

$$\begin{cases} A_n=0 \\ B_n=-\frac{1}{\varepsilon_0}\frac{nb^{2n+1}}{(2n+1)R_{\mathrm{SC}}^{n+1}}. \end{cases} \tag{A9}$$

Substituting (A9) to (A3) gives

$$U(\mathbf{r})=-\frac{1}{\varepsilon_0}\sum_{n=0}^{\infty}\frac{nb^{2n+1}}{(2n+1)R_{\mathrm{SC}}^{n+1}}\frac{1}{r^{n+1}}P_n(\cos\theta). \tag{A10}$$

Then the potential at $E$ is

$$U(\mathbf{r}_{\mathrm{E}})=-\frac{1}{b\varepsilon_0}\sum_{n=0}^{\infty}\frac{n}{2n+1}\left(\frac{b^2}{R_{\mathrm{EC}}R_{\mathrm{SC}}}\right)^{n+1}P_n(\cos\theta_{\mathrm{C}}). \tag{A11}$$

According to (A2), $U(\mathbf{r}_{\mathrm{E}})$ can also be written as

$$U(\mathbf{r}_{\mathrm{E}})=\frac{1}{4\pi\varepsilon_0}\iint_{\partial\Omega_2}\frac{\partial R_{\mathrm{SQ}}(\mathbf{r}_{\mathrm{Q}})}{\partial\mathbf{n}}\cdot\mathbf{n}\frac{\mathrm{d}\left(\partial\Omega_2\right)}{R_{\mathrm{SQ}}^2(\mathbf{r}_{\mathrm{Q}})R_{\mathrm{EQ}}(\mathbf{r}_{\mathrm{Q}})}. \tag{A12}$$

One can find (A1) equating the right hand sides of (A11) and (A12). □

# 2 Lemma 2.

If $\partial\Omega_2$ is an infinity plane in $\mathbb{R}^3$, $Q$ is an arbitrary point on $\partial\Omega_2$ and $S$, $E$ are arbitrary points share the same distance $h_1$ to plane $\partial\Omega_2$ as shown in Figure B1, then

$$-\frac{1}{2\pi}\iint_{\partial\Omega_2}\frac{\partial R_{\mathrm{SQ}}(\mathbf{r}_{\mathrm{Q}})}{\partial\mathbf{n}}\cdot\mathbf{n}\frac{\mathrm{d}\left(\partial\Omega_2\right)}{R_{\mathrm{SQ}}^2(\mathbf{r}_{\mathrm{Q}})R_{\mathrm{EQ}}(\mathbf{r}_{\mathrm{Q}})}=\frac{1}{\sqrt{R_{\mathrm{SE}}^2+4h_1^2}}. \tag{B1}$$

*Proof.* We follow a similar procedure as we did in Lemma 1. First, we establish a Cartesian coordinates $(x,y,z)$ in $\mathbb{R}^3$ with origin $S$ at $\mathbf{r}_{\mathrm{S}}:=(0,0,0)$. We then place $E$ at $\mathbf{r}_{\mathrm{E}}:=(0,R_{\mathrm{SE}},0)$ on the $y$-axis and $\partial\Omega_2$ as the normal plane of $z$-axis. The position $Q$ is defined with coordinates $\mathbf{r}_{\mathrm{Q}}:=(x,y,-h_1)$ on the plane $\partial\Omega_2: z=-h_1$. $R_{\mathrm{SE}}$ is the distance between $S$ and $E$. Next, we introducing the same charge density distribution function $q(\mathbf{r}_{\mathrm{Q}})$ on the plane $\partial\Omega_2$ as in Lemma.1. According to (A2), $U\left(\mathbf{r}_{\mathrm{E}'}\right)$ can be expressed as

$$U\left(\mathbf{r}_{\mathrm{E}'}\right)=\frac{1}{4\pi\varepsilon_0}\int_{-\infty}^{\infty}\int_{-\infty}^{\infty}-\frac{\partial R_{\mathrm{SQ}}(\mathbf{r}_{\mathrm{Q}})}{\partial h_1}\frac{\mathrm{d}x\mathrm{d}y}{R_{\mathrm{SQ}}^2(\mathbf{r}_{\mathrm{Q}})R_{\mathrm{QE}'}(\mathbf{r}_{\mathrm{Q}})}, \tag{B2}$$

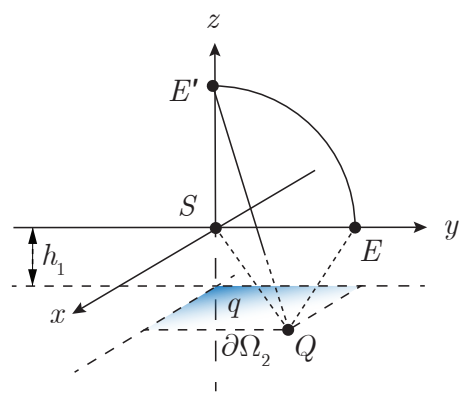


Figure B1: Auxiliary model of charged plane $\partial\Omega_2 : z = -h_1$ in vacuum. The position $Q$ has coordinates $\mathbf{r}_{\mathrm{Q}} := (x, y, -h_1)$ is an arbitrary point on the plane. The charge density $q(\mathbf{r}_{\mathrm{Q}})$ is distributed on $\partial\Omega_2$. Positions $S$, $E$ and $E'$ have coordinates $\mathbf{r}_{\mathrm{S}} := (0,0,0)$, $\mathbf{r}_{\mathrm{E}} := (0, R_{\mathrm{SE}}, 0)$ and $\mathbf{r}_{\mathrm{E}'} := (0, 0, R_{\mathrm{SE}})$ in the vacuum, which satisfy the line segments $|ES| = |E'S|$.

where

$$R_{\mathrm{SQ}}(\mathbf{r}_{\mathrm{Q}}) = \sqrt{x^2 + y^2 + h_1^2}$$

and

$$R_{\mathrm{QE}'}(\mathbf{r}_{\mathrm{Q}}) = \sqrt{x^2 + y^2 + (R_{\mathrm{SE}} + h_1)^2}.$$

Then, (B2) can be simplified as

$$U(\mathbf{r}_{\mathrm{E}'}) = -\frac{1}{2\varepsilon_0}\frac{1}{2h_1 + R_{\mathrm{SE}}}. \tag{B3}$$

Equation (B3) can be rewritten using Taylor series as

$$U(\mathbf{r}_{\mathrm{E}'}) = \begin{cases} -\frac{1}{2\varepsilon_0}\sum_{n=0}^{\infty}\frac{(-1)^n 2^n h_1^n}{R_{\mathrm{SE}}^{n+1}} & \text{if } 2h_1 < R_{\mathrm{SE}} \\ -\frac{1}{2\varepsilon_0}\sum_{n=0}^{\infty}\frac{(-1)^n R_{\mathrm{SE}}^n}{2^{n+1} h_1^{n+1}} & \text{if } 2h_1 > R_{\mathrm{SE}}. \end{cases} \tag{B4}$$

Comparing (B4) with (A3) we have

$$\begin{cases} A_n = 0, B_n = -\frac{1}{2\varepsilon_0}(-1)^n 2^n h_1^n & \text{if } 2h_1 < R_{\mathrm{SE}} \\ A_n = -\frac{1}{2\varepsilon_0}\frac{(-1)^n}{2^{n+1} h_1^{n+1}}, B_n = 0 & \text{if } 2h_1 > R_{\mathrm{SE}}. \end{cases} \tag{B5}$$

The position $\mathbf{r}_{\mathrm{E}}$ can also be re-written as $(R_{\mathrm{SE}}, \pi/2, 0)$ in spherical coordinates. Substituting (B5) into (A3) then gives

$$U(\mathbf{r}_{\mathrm{E}}) = \begin{cases} -\frac{1}{2\varepsilon_0}\sum_{n=0}^{\infty}\frac{(-1)^n 2^n h_1^n}{R_{\mathrm{SE}}^{n+1}} P_n(0) & \text{if } 2h_1 < R_{\mathrm{SE}} \\ -\frac{1}{2\varepsilon_0}\sum_{n=0}^{\infty}\frac{(-1)^n R_{\mathrm{SE}}^n}{2^{n+1} h_1^{n+1}} P_n(0) & \text{if } 2h_1 > R_{\mathrm{SE}}. \end{cases} \tag{B6}$$

Since the Legendre polynomials can be expressed in differential form, namely

$$P_n(x) = \frac{1}{2^n n!} \frac{\mathrm{d}^n}{\mathrm{d}x^n} \left[ \left( x^2 - 1 \right)^n \right],$$

we have that

$$P_n(0) = \begin{cases} \frac{(-1)^m}{2^{2m}} \frac{(2m)!}{(m!)^2} & \text{for} \quad n = 2m \\ 0 & \text{for} \quad n = 2m+1. \end{cases} \tag{B7}$$

From Taylor series we have

$$\frac{1}{\sqrt{1+x}} = \sum_{m=0}^{\infty} \frac{(-1)^m}{2^{2m}} \frac{(2m)!}{(m!)^2} x^m \tag{B8}$$

when $|x| < 1$. Substituting (B7) and (B8) into (B6) gives

$$U(\mathbf{r}_{\mathrm{E}}) = -\frac{1}{2\varepsilon_0 \sqrt{R_{\mathrm{SE}}^2 + 4h_{\mathrm{I}}^2}}. \tag{B9}$$

One can find (B1) equating the right hand sides of (B9) with (A12). □